SUPPLEMENTARY INFORMATION

Rietveld refinements of the high-resolution synchrotron XRD patterns of the mechanically milled $ZrNiSn_{1-x}Sb_x$ samples revealed the presence of several secondary phases, including Sn, Ni_3Sn_4, $NiZr_2$, $Ni_{2.7}Sn_2$, and $Ni_{0.92}Sn_{0.08}$. Among all compositions and milling conditions investigated, the alloy milled for 20 h exhibited the highest total fraction of secondary phases, amounting to approximately 17%. Within this fraction, Ni_3Sn_4 was the dominant impurity phase (see Table 1 for a detailed phase quantification).

The presence of Ni_3Sn_4 was further corroborated by HRTEM analyses (Fig. 3), where nanometric precipitates of this phase were observed coexisting with ZrNiSn nanocrystals. The lattice fringes corresponding to Ni_3Sn_4 in the HRTEM images exhibit d-spacings that are in good agreement with theoretical values; any small deviations fall within the expected range for nanostructured precipitates and can be attributed to strain and size effects arising from the mechanical milling process.

In the synchrotron XRD pattern of the 20 h milled sample (Fig. 1), the most intense reflection of the Ni_3Sn_4 phase is depicted, corresponding to the (111) plane. In contrast, the HRTEM image displays lattice fringes associated with the $(\bar{3}11)$ planes of Ni_3Sn_4, a difference that arises from the specific crystallographic orientation of the nanocrystal with respect to the incident electron beam.

Table S1. *Calculated Bragg peak positions for the Ni_3Sn_4 intermetallic phase (space group* C2/m*). The table lists the Miller indices (hkl), interplanar spacing d and relative intensities. Reflections are sorted by decreasing d-spacing down to 1.3 Å. Reflections depicted in Figure 1 and Figure 3 are highlighted in **green** and **yellow**, respectively. Those reflections with lower relative intensity than 2% have been omitted. Errors in the d-spacings are in the last significant figure.*

h	k	l	d (Å)	Relative intensity (I/I_{max})
2	0	0	5.980937	5.9
0	0	1	5.063198	2.7
1	1	1	2.951857	100.0
-4	0	1	2.886638	48.0
3	1	0	2.840235	50.5
-3	1	1	2.673984	17.9
-2	0	2	2.555155	6.9
0	0	2	2.531599	21.5
4	0	1	2.346313	21.2
3	1	1	2.318167	25.0
-4	0	2	2.202121	2.2
2	0	2	2.157636	24.2
-3	1	2	2.068283	87.8

5	1	0	2.057301	56.6
1	1	2	2.043402	13.1
0	2	0	2.023383	47.3
-6	0	1	2.022884	10.4
-6	0	2	1.781259	3.3
-2	0	3	1.733448	6.8
6	0	1	1.723032	2.2
0	0	3	1.687733	2.4
-4	2	1	1.656882	17.6
-7	1	1	1.604186	6.0
-2	2	2	1.589089	3.1
-0	2	2	1.580574	4.8
7	1	0	1.570012	2.9
4	2	1	1.534558	10.8
1	1	3	1.503741	12.7
8	0	0	1.489936	5.5
-7	1	2	1.487939	2.1
2	2	2	1.475929	13.0
-6	0	3	1.468081	3.2
5	1	2	1.456664	11.1
-8	0	2	1.443319	8.2
-6	2	1	1.430571	5.9
7	1	1	1.419254	3.7
6	0	2	1.414096	2.1
8	0	1	1.341894	3.0
-6	2	2	1.340426	2.4
4	0	3	1.336992	2.3
-2	2	3	1.316415	5.1
-2	0	4	1.301403	3.9

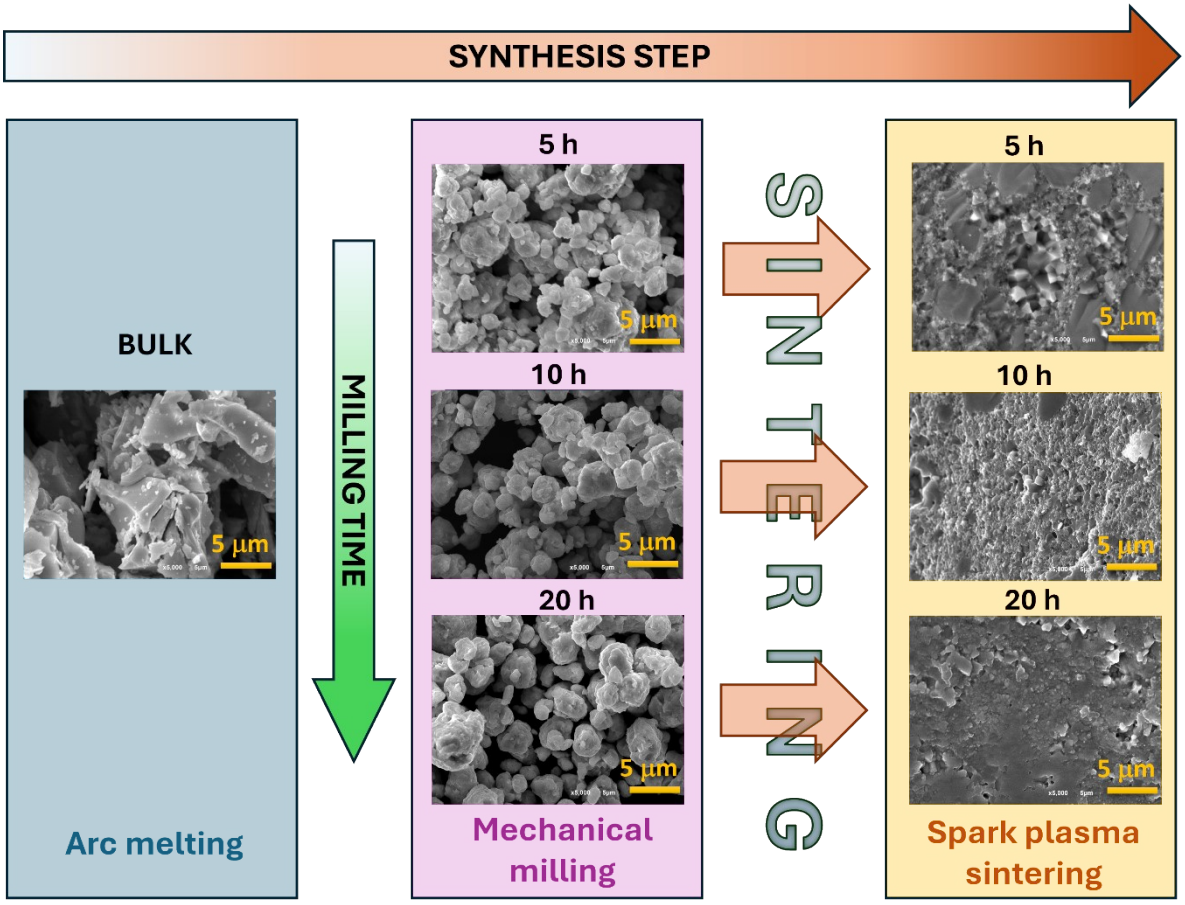

Figure S1. *Synthesis route and resulting microstructures of the ZrNiSn-based samples. The ingot obtained by arc melting (left) was subjected to high-energy mechanical milling for different milling times, producing progressively refined and agglomerated powders (middle). The milled powders were consolidated by spark plasma sintering (right), yielding dense polycrystalline pellets. Representative SEM micrographs corresponding to each stage illustrate the morphological evolution from the as-cast bulk microstructure to the nanostructured milled powders and the fracture surface of the final sintered compacts.*

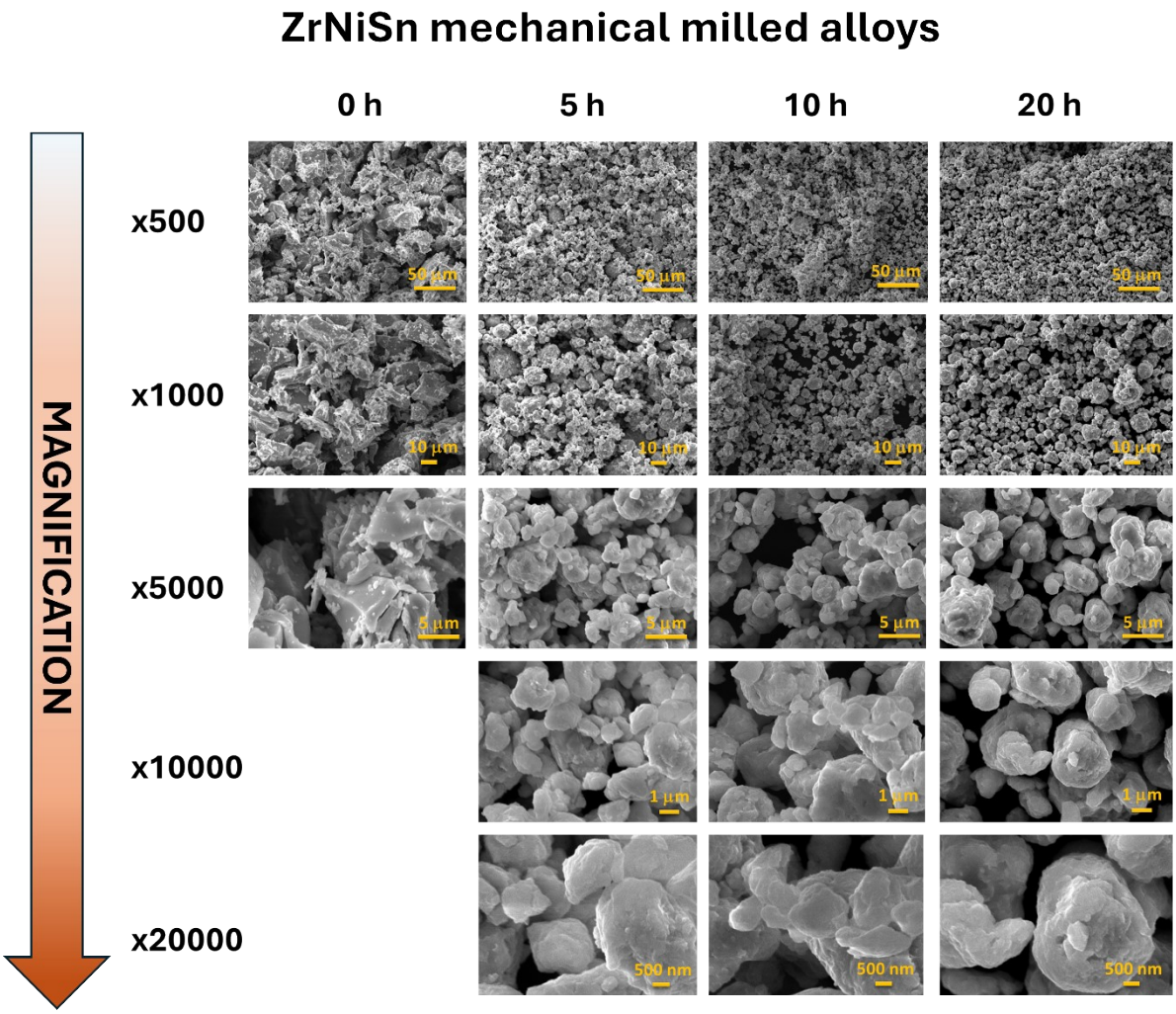

Figure S2. *SEM micrographs showing the evolution of the microstructure in ZrNiSn samples subjected to different mechanical-milling durations (0, 5, 10, and 20 h). Images are presented at various magnifications to highlight both the global morphology and the fine-scale features. The reference sample (0 h) exhibits a coarse and relatively inhomogeneous grain morphology. After 5 h of milling, clear grain refinement and decreased surface roughness become evident. Prolonged milling for 10 and 20 h leads to further fragmentation and agglomeration of nanoparticles. The progressive microstructural refinement and defect accumulation are consistent with the high-energy ball-milling process and correlate with the changes observed in the thermoelectric transport properties.*